Effects of Fe, Mn and chemical grain refinement and cooling rate on the evolution of Fe intermetallics in a model 6082 Al-alloy

M. H. Khan[a,*], A. Das[b], Z. Li [a], H.R. Kotadia[a,]**

[a]WMG, University of Warwick, Coventry, CV4 7AL, UK

[b]College of Engineering, Swansea University, Bay Campus, Swansea, SA1 8EN, UK

* mir-hamza.khan@warwick.ac.uk (M. H. Khan), ** H.Kotadia@warwick.ac.uk (H. Kotadia)

Abstract: The solidification microstructures formed in a model 6082 alloy with 0.2-1.0 wt. % Fe were examined under different cooling rates and the effects of 0.5 wt. % Mn and Al-5Ti-1B grain refiner addition investigated. The results were compared against Thermo-Calc, differential scanning calorimetry (DSC) and cooling curve analysis. Fe promotes primary-Al grain refinement from growth restriction and constitutional undercooling effects but increases detrimental β–($Al_9Fe_2Si_2$) intermetallic. Mn contributes to primary-Al grain refinement from growth restriction and promotes the formation of α–$Al_{15}(Fe,Mn)_3Si_2$ at the expense of increased intermetallic content. Al-5Ti-1B inoculation not only produces the strongest refinement of primary-Al grains but also refines the Fe-intermetallics by enhancing their nucleation and restricting their growth volume in the interdendritic liquid pockets.

Keywords: Aluminium alloys; Iron intermetallics; Solidification; Microstructure modification; Grain refinement.

1. Introduction

Aluminium alloys have become attractive structural materials because of its one third the density of steel and excellent specific strength (strength/density), formability, crash resistance and corrosion resistance [1]. This makes Al particularly attractive in the transportation industries for light-weighting and reduction of CO_2 emission. Heat treatable wrought 6xxx (Al-Mg-Si) Al-alloys exhibit moderate high strength (> 300 MPa) with excellent corrosion resistance and extrudability, making them attractive for Body-in-White (BIW) application [2]. However, continuous increase in Al usage in automotive applications also warrants increased recycling of Al alloys and achieve ~95% of energy saving (as compared to primary Al production) [3, 4]. Currently, only around 20 % of end-of-life scrap is recycled into wrought products, even though wrought alloys account for two-thirds of all Al in use [5, 6]. The limitation is due to sensitivity of wrought Al to residual elements such as Fe, Si and Cu, which accumulate during recycling. The presence of unwanted elements degrade mechanical and corrosion performance of recycled wrought-Al [1, 7].

The accumulation of Fe originates from bauxite ores, master alloys, fabrication process and poor scrap separation, which increases the Fe concentration to 0.2-1.0 wt. % [8]. This concentration is sufficient to form Fe-based intermetallic compounds (Fe-IMCs), as Fe has negligible solid solubility (max. 0.04 wt. %) in Al [9]. The Fe-IMCs have a detrimental effect on the mechanical properties (e.g. fatigue life and ductility) and corrosion resistance [10, 11]. Since, Fe cannot be economically removed from molten Al, strategies have been developed to neutralize its negative effects. Three methods have been reported: (i) alloying addition such as Mn, which modifies the detrimental β–$Al_9Fe_2Si_2$ (needle shape) to α– $Al_{15}(Fe,Mn)_3Si_2$ (Chinese-script and/or compact shape) IMC [12-14], (ii) using physical force such as ultrasonication [15-17], intensive shearing [18-20] or electromagnetic stirring [21, 22] to modify the morphology and overall distribution of Fe-IMCs , and (iii) controlling processing parameters, such as cooling rate, during casting [23, 24] or heat treatment to modify the IMCs [25]. Among these methods, the chemical route is the most widely adopted due to its ease of application and lower cost.

Alloying elements and inoculant particles can have three major effects on Fe-IMCs. Firstly, they can alter the nucleation and growth characteristics of IMCs. Secondly, the mechanical and chemical properties may change due to modification of the structure or morphology of phases (e.g., formation of α–Al_8Fe_2Si instead of β–$Al_9Fe_2Si_2$). Thirdly, they can form additional IMCs.

The chemical additions can be divided roughly into two major categories: (i) alloying elements such as, Ti, V, Cr, Mn, Co, Ni, Sr are selectively used to alter the growth of Fe-IMCs through acting as kink blockers, surfactants, incorporates or step pinner [26-29] and (ii) particles such as, Al_2O_3, MgO, AlP, TiB_2 to influence the nucleation and growth of IMCs [30-33]. The elements belonging to category (i) usually have the most pronounced effect on IMC development. However, these elements also form sludge [34] and consequently increase IMC volume fraction causing further deterioration of mechanical properties. While considerable amount of study has been conducted on the primary-Al grain refining and eutectic-Si modification, the correlation between primary-Al refinement and morphological evolution of Fe-IMC has largely been overlooked.

The main objective of this study is to understand how the addition of solute elements and grain refiners alter the formation of the Fe-IMCs. The effects of cooling rates, chemical grain refinement, and the influence of primary-Al on the formation and distribution of the IMCs in the as-cast microstructure has been investigated. Effects of varying Fe (from 0.2 – 1.0 wt. %) and Mn (with a Mn/Fe ratio of 0.5) contents and of Al-5Ti-1B grain refiner (1gm/1kg) have been investigated in a model 6082 Al-alloy to understand how primary-Al microstructure affects Fe-IMC morphology and distribution.

2. Experimental Procedure

2.1 Alloy preparation

In this study a model 6082 Al-alloy is prepared by melting commercially pure Al (99.87 wt. %) in a clay-graphite crucible inside an electrical resistance furnace and adding appropriate hardeners (e.g., Al-20Mg, Al-20Si, Al-10Fe, all expressed in wt.%). The melt was homogenised for at least two hours at 740 °C (± 3 °C) with intermittent stirring to achieve homogeneity. For experiments involving chemical grain refinement, a pre-measured quantity of Al-5Ti-1B master alloy was added to the melt at 1gm/kg ratio (industry limit) 5 minutes prior to casting. Compositions of the prepared alloys were verified through optical emission spectroscopy (Foundry Master Pro) and presented in Table 1.

Table 1. Chemical composition (in wt. %) of the model 6082 alloy used in this study.

Alloy designation	Al	Mg	Si	Fe	Mn	GR (Al-5Ti-1B)
6082/ Reference/0.2Fe	Balance	0.95	1.24	0.21		
0.5Fe	Balance	0.95	1.22	0.52		
0.8Fe	Balance	0.95	1.23	0.78		
1Fe	Balance	0.95	1.21	1.1		
1Fe-0.5Mn	Balance	0.95	1.20	1	0.46	
1Fe + GR	Balance	0.95	1.22	1		✓
1Fe-0.5Mn + GR	Balance	0.95	1.19	1.1	0.45	✓

2.2 Solidification experiments

To study the effects of solute elements and grain refiner under different cooling rates, a purpose-built Cu wedge mould was used (Fig. 1). All solidification experiments were conducted under identical casting conditions. The solidified billets were sectioned along the central vertical plane for metallographic investigation. The samples from the regions of fast and slow cooling were investigated. For Differential Scanning Calorimeter (DSC) experiments, samples from the fast cooled region were used to minimise effects of segregation.

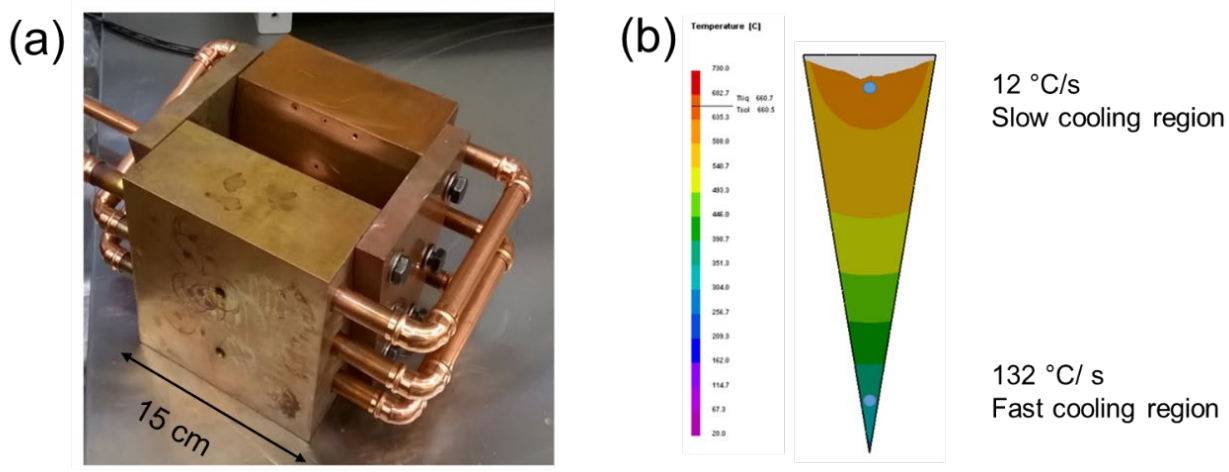

Fig. 1. (a) Copper wedge shape mould and (b) Cooling rate predicted by ProCAST, top region with slow cooing rate (12 °C/s) and tip of the mould shows fast cooling (132 °C/s). .

2.3 Investigation of phase equilibria

The phase transformation and nucleation temperatures of primary-Al and Fe-IMCs are investigated through the analysis of cooling curves obtained using a K-type thermocouple connected to a multi-channel data logger (Micro-Measurements System 8000) operating at 100 Hz and through differential scanning calorimetry (DSC) analysis using a NETZSCH STA449 F3. In each DSC experiment, ~20 mg sample is placed in an alumina crucible and heated/cooled between 100 °C and 750 °C at 5 °C min^{-1}. Both DSC and cooling curve experiments were repeated multiple times to ensure reproducibility. Thermal analysis results were analysed against solidification curves and property diagrams calculated using Thermo-Calc software (TCAL 4: Mobile v4.0 and MOBALE3: Al-Alloys Mobility v3.0 packages).

2.4 Sample characterisation

For microstructural analysis, samples were ground and polished following standard metallographic techniques using SiC abrasive papers, diamond paste, and finally polished using 0.25 µm colloidal silica suspension. Preliminary microstructural analysis was conducted using ZEISS Axioscop2 MAT optical microscope equipped with AxioVision image capture software. Fe-IMCs were investigated using JEOL 7800F SEM equipped with EDS and EBSD detectors (Oxford Instrument). Backscattered electron (BSE) detector was used for better image contrast. The specimens were also anodized using Barkers reagent (8 ml HBF_4 and 92 ml H_2O) for approximately 1 minute at 20 V for polarised light microscopy. The mean linear intercept method (Fig. 2a) is used for primary-Al grain size measurement. Selected samples were deep-etched using 37% HCl for 60 s to reveal the 3D morphology of the Fe-IMCs. SEM images are used to measure the β–($Al_9Fe_2Si_2$) Fe IMCs platelet size (Fig. 2b). The α–$Al_{15}(Fe,Mn)_3Si_2$ (Chinese-script) IMC distribution is validated through the quadrant method [35] by carefully selecting the quadrant size approximately twice the size of the mean area per IMC (Fig. 2c). The degree of asymmetry of a statistical distribution around its mean can be quantified by its skewness B, which is defined by:

$$B = \frac{q}{(q-1)(q-2)} \sum \left[\frac{N_{qi} - N_q^{mean}}{\sigma}\right]^3 \quad (1)$$

where q is the total number of quadrats studied, N_{qi} is the number of Chinese-script particles in the ith quadrant (i = 1, 2,…..,q), N_q^{mean} is the mean number of Chinese-script particles per quadrat, and σ is the standard deviation of the N_q distribution. The increase in B indicates an increase in heterogeneity and non-uniform microstructure.

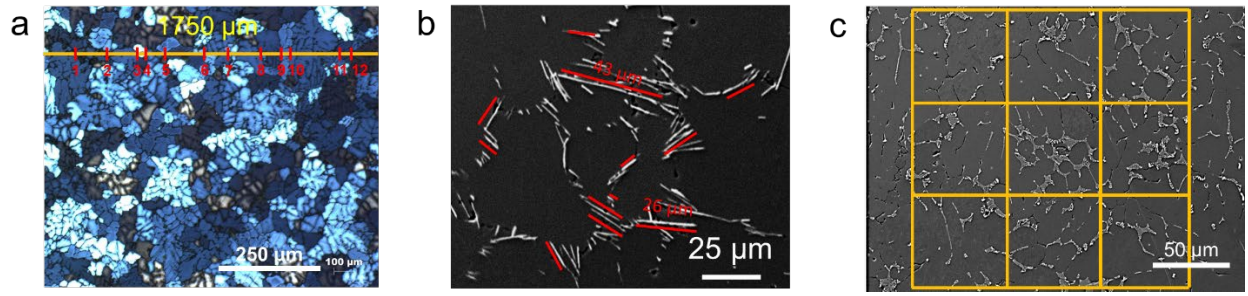

Fig. 2. The statistical analysis methods: (a) the linear intercept method on polarised light micrograph, (b) the line measuring the β–($Al_9Fe_2Si_2$) Fe IMCs platelet size, and (c) the quadrant method on low magnified SEM micrograph.

3. Results

3.1 Solidification microstructure of primary-Al

Figure 3 shows microstructures of samples from the fast and slow cooled regions of the wedge-shaped billets. Well-developed dendritic microstructures are observed in the slow-cooled region and very fine dendritic structures are observed in the fast-cooled region. The 1%Fe sample with the addition of 0.5%Mn and Al-5Ti-1B master alloy shows substantial reduction in grain size throughout, as evidenced in the microstructure (Fig. 3vi and vii) and macrostructure (Fig. 3d) from the ingot. The average grain size from the slow (top) and fast cooling (bottom) region of the ingots are plotted as a function of alloying addition in Fig. 3b. Larger grain sizes are observed in the slow cooled regions for all alloys since slow solidification of Al in this region leads to only the largest size nucleants being used and due to considerable growth of the grains. There is a gradual reduction in the grain size, consistent with the increase in cooling rate, from the top to the bottom of the wedge mould for all seven alloys.

Without chemical inoculation there is a mild progressive refinement of primary–Al grains with an increase in Fe content from 0.2 to 1.0%. Chemical inoculation (with Al-5Ti-1B) leads to significant refinement of primary–Al grains throughout the ingots as shown in Fig. 3 for 1Fe+GR and 1Fe-0.5Mn+GR alloys. The grain sizes observed under chemical inoculation shows marginal difference between slow or fast cooling conditions.

The reference alloy with 0.2% Fe consist of well-developed coarse dendritic grains with an average grain size of ~220 and 125 µm in the slow and fast cooling regions, respectively. As the Fe content increases from 0.2 to 1.0%, microstructural refinement results from the solute effect. Fine and equiaxed grain structures are observed after the addition of inoculant with an

average grain size ranging between 80 to 120 μm throughout the entire ingot. Adding Fe, Mn and grain refiner together leads to the finest grain structure as compared to the addition of just Fe and Mn. Though the addition of Mn into the melt refines the primary–Al grains, this does not appear to result from Mn alone and is contributed by the total solute content including Fe and Mn as observed by the trend in the grain size plot (Fig. 3). The average grain sizes and the average grain density calculated in the ingots (assuming space-feeing geometry of spherical grains) are also tabulated in Fig. 3c. Addition of Fe (0.2-1.0%) significantly increase the grain density in the reference alloy. The combined effect of Fe, Mn and chemical grain refiner increased the overall grain density to almost ~3 times in the fast-cooled (132^{o} C/s) region and ~ 8 times in slow-cooled (12^{o} C/s) region in comparison to the reference alloy (0.2Fe).

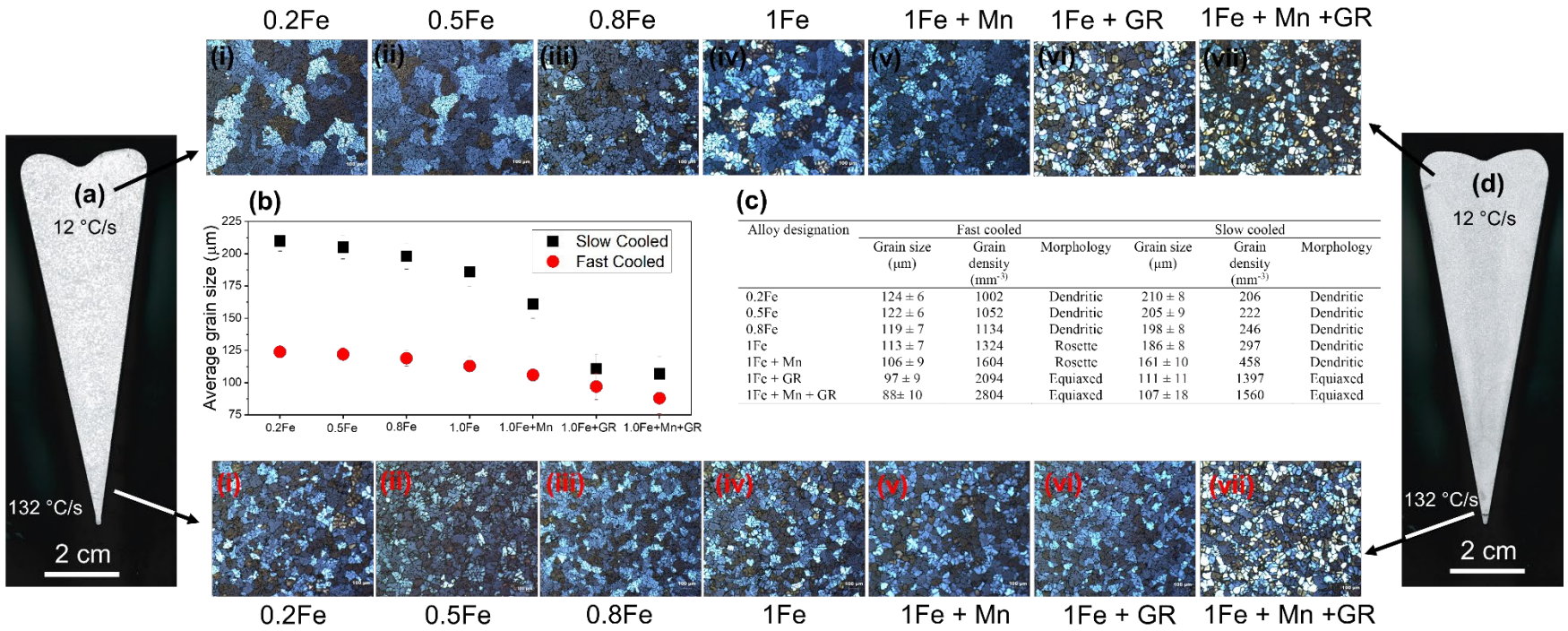

Alloy designation	Fast cooled			Slow cooled		
	Grain size (μm)	Grain density (mm^{-3})	Morphology	Grain size (μm)	Grain density (mm^{-3})	Morphology
0.2Fe	124 ± 6	1002	Dendritic	210 ± 8	206	Dendritic
0.5Fe	122 ± 6	1052	Dendritic	205 ± 9	222	Dendritic
0.8Fe	119 ± 7	1134	Dendritic	198 ± 8	246	Dendritic
1Fe	113 ± 7	1324	Rosette	186 ± 8	297	Dendritic
1Fe + Mn	106 ± 9	1604	Rosette	161 ± 10	458	Dendritic
1Fe + GR	97 ± 9	2094	Equiaxed	111 ± 11	1397	Equiaxed
1Fe + Mn + GR	88± 10	2804	Equiaxed	107 ± 18	1560	Equiaxed

Fig. 3. Polarised light micrographs from the 0.2 to 1.0 wt. %Fe alloy ingots: (a) macrostructure of 0.2 wt. % Fe reference wedge shaped ingot, (b) average grain size as a function of Fe, Mn and GR contents from the slow and fast cooling regions, (c) tabulated average grain size, grain density and morphology from fast (132 ºC/s) and slow cooled (12 ºC/s) condition for all ingots, and (d) macrostructure of 1.0 wt.%Fe-0.5 wt.%Mn + GR wedge shaped ingot.

3.2 Solidification of Fe intermetallics

Fig. 4 illustrates the morphologies of the IMCs in the fast and slow cooled regions of all seven alloys. Fig. 5 shows the morphology of β–$Al_9Fe_2Si_2$, α–$Al_{15}(Fe,Mn)_3Si_2$ and α–Al_8Fe_2Si IMCs formed in the 1.0 wt.% Fe alloys. The alloys with 0.2 to 1.0 wt.% Fe predominantly form β-$Al_9Fe_2Si_2$ with platelet length ranging from 2 to 50 μm in the slow-cooled (12 °C/s) and α–Al_8Fe_2Si with fibrous structures forms in fast-cooled (132 °C/s) . Increasing Fe content from 0.2 to 1.0 wt. % results in a rise in the volume fraction and length of β-$Al_9Fe_2Si_2$ plates in the slow cooled region (12° C/s). EDS and EBSD studies were conducted to identify the IMCs present in the as-cast microstructures, as presented in the next section.

Addition of Mn to the 1Fe alloy resulted in a noticeable change from platelet like β–$Al_9Fe_2Si_2$ to Chinese script α–$Al_{15}(Fe,Mn)_3Si_2$ (Figs. 4 and 5) formation. In Fig. 4, however, there is visible fibrous structures present in the fast-cooled region. The 1.0 wt. % Fe alloy shows a combination of β-$Al_9Fe_2Si_2$ and α–Al_8Fe_2Si IMCs following grain refiner (GR) addition. Addition of GR to 1Fe-0.5Mn alloy leads to smaller Chinese script IMCs evenly distributed across the as-cast microstructures (Figs. 4 and 5). Deep-etched microstructures, as shown in Fig. 5, present the 3D morphology of the IMCs, where the interconnectivity and distribution of the IMCs are revealed. The 3D morphology suggests that the IMCs grow around the grains and secondary dendritic arms. It appears that in the slow cooled regions the IMCs nucleate and develop in the eutectic pockets interspersed between the primary-Al dendrites. In the grain-refined alloys (1Fe+GR and 1Fe-0.5Mn +GR) the α–Al_8Fe_2Si and Mg_2Si growth is inhibited resulting in thinner IMC structures between the secondary dendritic arms of primary–Al.

The size and distribution of the Fe-IMCs, measured using the Quadrant method, are presented in Fig. 6b for different alloying addition. The size distribution of β–$Al_9Fe_2Si_2$ IMCs are compared in Fig.6a for the slow cooled regions of the ingots. Increase in Fe content appears to increase the size of β–$Al_9Fe_2Si_2$ IMCs and the spread in their size range. GR addition has reduced the IMC size and the spread in the distribution. Fig. 6b shows a comparison of α–$Al_{15}(Fe,Mn)_3Si_2$ IMC size distribution using quadrat method. Similar observations are made for the α–$Al_{15}(Fe,Mn)_3Si_2$ IMC particles in the 1Fe-0.5Mn alloys (Fig. 6b) where inoculation produces finer particles with a narrower size distribution. Results presented in Fig. 6c show that the IMC area fraction steadily increases with Fe content. There is significant increase in IMC area fraction with Mn addition highlighting that Mn addition promotes Fe-IMC formation in addition to converting β–$Al_9Fe_2Si_2$ into α–$Al_{15}(Fe,Mn)_3Si_2$. On the other hand, addition of grain refiner appears to increase IMC content in the absence of Mn but decreases the IMC

content in the presence of Mn. For all of the alloys, fast cooling resulted in larger area fraction of Fe-IMCs formed.

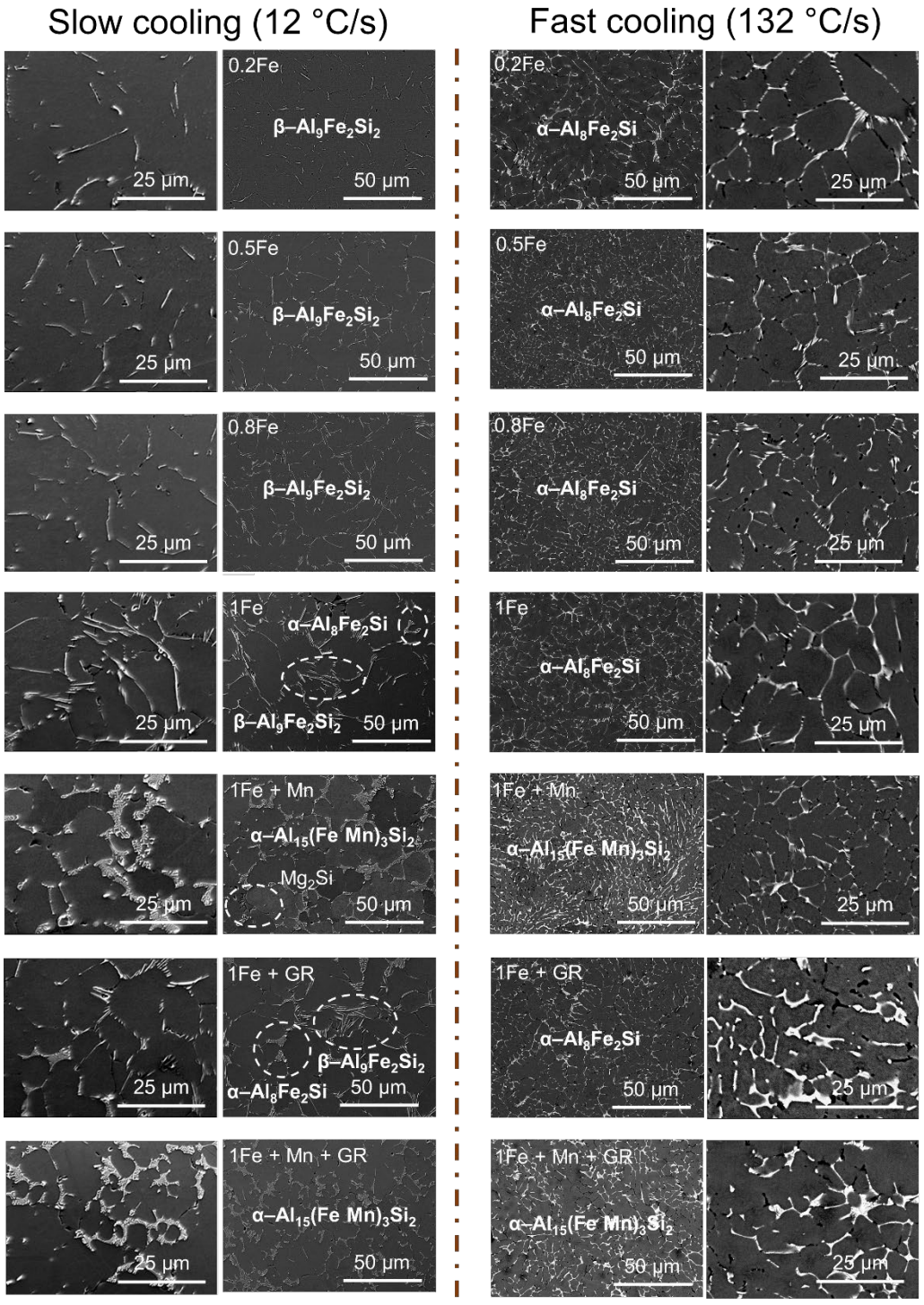

Fig. 4. SEM- BSE images from solidified ingots illustrating the variation in Fe-intermetallic size, distribution and morphologies with the cooling condition, Fe content and inoculant addition.

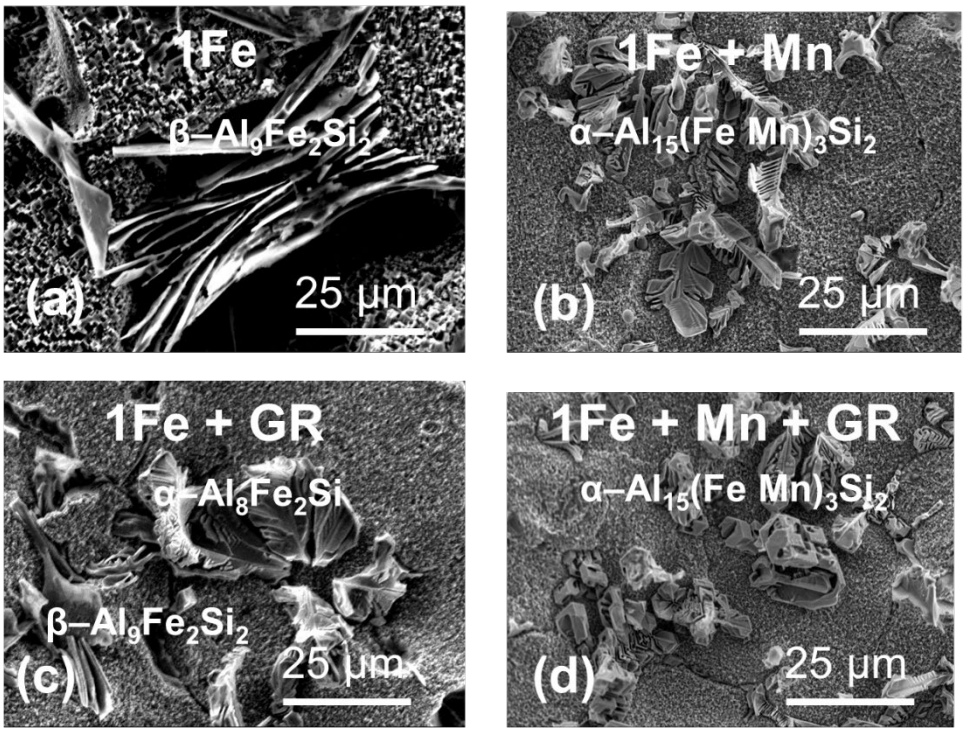

Fig. 5. Deep-etched microstructure (SEM-BSE) illustrating the morphology of β–$Al_9Fe_2Si_2$ and α–$Al_{15}(Fe,Mn)_3Si_2$ IMCs formed in (a) 1.0 wt.% Fe, (b) 1.0 wt.% Fe - 0.5 wt.% Mn (Fe: Mn ratio 0.5), (c) Al-5Ti-1B inoculated 1.0 wt.% Fe, and (d) inoculated 1.0 wt.% Fe - 0.5 wt.% Mn alloy.

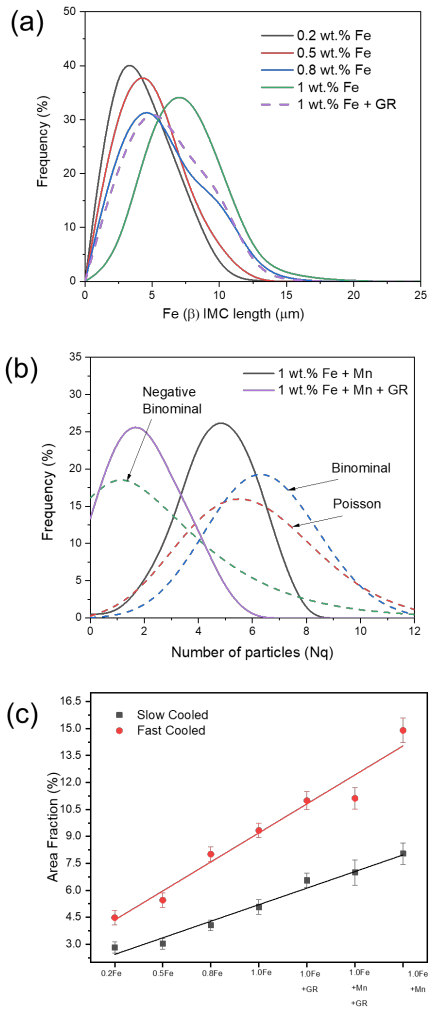

Fig. 6. Variation in Fe-IMC size and distribution, as determined by the Quadrant method, in different alloys: (a) size distribution of β–$Al_9Fe_2Si_2$ IMC from the slow cooled region, (b) distribution of Chinese-script α-$Al_{15}(Fe,Mn)_3Si_2$ IMC under slow cooling in the 1.0 wt. %Fe-0.5 wt.%Mn alloy in the presence and absence of inoculation, and (c) area fraction of Fe-IMCs (α and) from the slow and fast cooling regions.

3.3. Fe-IMC identification through EBSD analysis

Fig. 7 presents EBSD maps identifying the Fe-IMCs. For all alloys the monoclinic β-$Al_9Fe_2Si_2$ and cubic α-$Al_{15}(Fe,Mn)_3Si_2$ were investigated. EBSD analysis was confined to the four alloys containing 1.0 wt.% Fe as they contain the largest fraction of Fe-IMCs. Corby and Black [36] investigated the Al-Fe-Si system identifying the hexagonal α-Al_8Fe_2Si with space group $P6_3/mmc$ with lattice parameters a = 1.24 nm and c = 2.62 nm. The cubic α–$Al_{15}(Fe,Mn)_3Si_2$ was analogous to α-$Al_{17}(Fe,Mn_{3.5})Si_2$, found by Cooper *et al.* [37] with a space group of $Pm\text{-}3$ and lattice parameter of a = 12.56 nm. Various other compositions for this phase were found comprising $Al_{12}(Fe,Mn_3)Si_2$ [38] and $Al_{15}(Fe,Mn_3)Si_2$ [39]. It should be noted that both Mn containing alloys contained α–$Al_{15}(Fe,Mn)_3Si_2$ phase resulting from some conversion from β to α phase as also confirmed through thermodynamic calculations (discussed in the following section). The β-$Al_9Fe_2Si_2$ exhibits twinning resulting in a distorted monoclinic structure, as reported by Mondolfo [39] and Romming *et al.* [40], with a space group $A2/a$ with lattice parameters of a = 0.626 nm, b = 0.6175 nm, c = 2.0813 nm and β-90.42 (3)°.

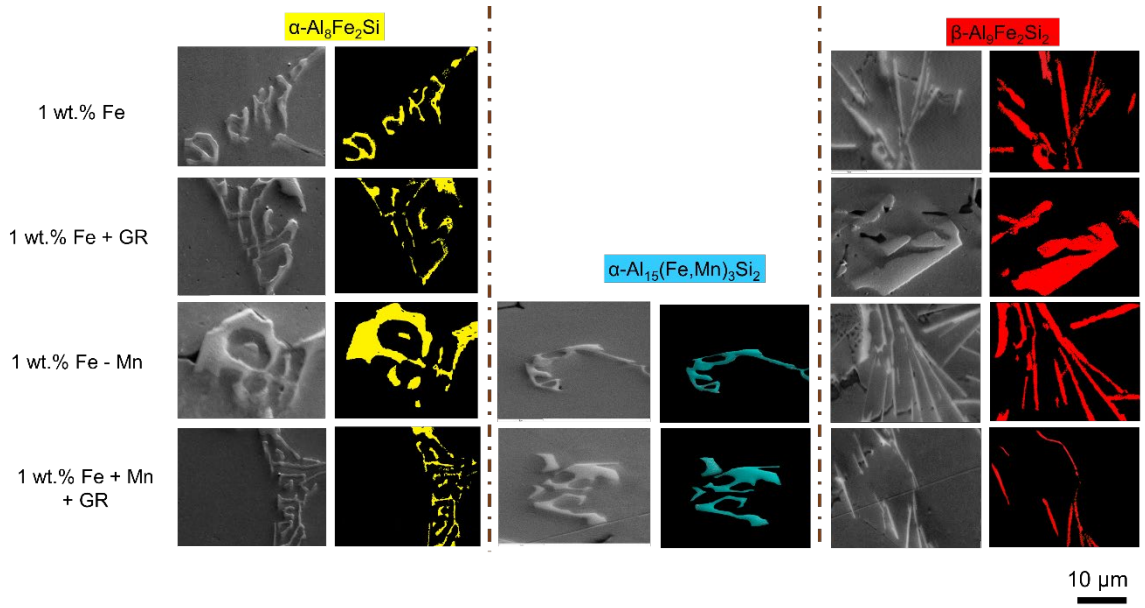

Fig. 7. SEM micrographs and EBSD phase mapping showing the hexagonal α-Al_8Fe_2Si, cubic α–$Al_{15}(Fe,Mn)_3Si_2$ and monoclinic β-$Al_9Fe_2Si_2$ IMC phase in 1.0 wt. % Fe from the slow cooled region (12 °C/s).

3.4 Solidification sequence of phases

To understand the microstructural evolution in the alloys, the solidification sequences have been evaluated using Thermo-Calc software and TCAL4 database. As microstructural observation (Fig .4 and 5) and quantitative analysis showed that β-$Al_9Fe_2Si_2$ phase increases with an increase in Fe content, phase evolution is investigated only in the alloy with highest Fe content. Figs. 8 a-b show the phase fraction evolution in the 1Fe and 1Fe-0.5Mn alloys under equilibrium solidification. The observed microstructures are in qualitative agreement with the predictions. According to Thermo-Calc, the five major phases predicted to form during solidification are: primary-Al, α–Al_8Fe_2Si, β-$Al_9Fe_2Si_2$, α-$Al_{15}(Fe,Mn)_3Si_2$, and Mg_2Si. Thermo-Calc also predicts the formation and subsequent dissolution of small amount of $Al_{13}Fe_4$ with none remaining in the solidified microstructure.

In the 1Fe alloy (Fig. 8a), primary-Al is the first phase to solidify starting at 645 °C and constitutes the major component in the alloy. $Al_{13}Fe_4$ starts solidifying at 636 °C with slow increase in phase fraction till 619 °C. α–Al_8Fe_2Si starts forming at 619 °C initially with a rapid increase in fraction that coincides with rapid dissolution of $Al_{13}Fe_4$ along with a sudden increase in α-Al fraction and decrease in liquid fraction. This indicates α–Al_8Fe_2Si formation through a eutectic reaction that also dissolves any $Al_{13}Fe_4$ in the microstructure. This is followed by a slow increase in the α–Al_8Fe_2Si fraction till 597 ºC and a rapid decrease and complete dissolution by 595 ºC. The dissolution of α–Al_8Fe_2Si coincides with β-$Al_9Fe_2Si_2$ solidification (597 °C) with a concurring drop in liquid level and increase in α-Al indicating another eutectic reaction. Very small amount of Mg_2Si, the last phase to solidify, starts forming at 550 °C. The addition of Mn significantly changes the Thermo-Calc predictions. α–Al_8Fe_2Si phase is completely suppressed and replaced by the formation of Chinese-script α–$Al_{15}(Fe,Mn)_3Si_2$ nucleating at 635 ºC and steadily growing into the largest intermetallic remaining in the solidified microstructure. β-$Al_9Fe_2Si_2$ starts nucleating at a slightly lower temperature of 582 ºC and the amount of β remains quite low in the final microstructure with Mn addition. Unlike in the alloy without Mn, both α-IMC and β-IMC fraction increase gradually and no sudden changes in the α-Al and liquid fractions are observed to coincide with their solidification. This might indicate that Mn promotes direct solidification of Fe IMCs from the interdendritic liquid without any eutectic reaction.

For a more accurate understanding of solidification of the samples in the experiments, DSC scans were performed and compared with the Thermo-Calc predictions for all alloys containing

1.0 wt.% Fe. The DSC scans, presented in Fig. 8c, confirm the solidification of three major phases: primary–Al, α–Al_8Fe_2Si/α–$Al_{15}(Fe,Mn)_3Si_2$ and β-$Al_9Fe_2Si_2$. Primary–Al solidification constitutes the largest peak with a nucleation temperature around 650 °C, followed by peaks for α–Al_8Fe_2Si/α–$Al_{15}(Fe,Mn)_3Si_2$ and β-$Al_9Fe_2Si_2$ formation around temperatures of 635 °C and 580 °C, respectively. There are slight variations in the formation temperatures of IMCs between the alloys. In samples containing Mn, the α-IMC solidification peak becomes stronger indicating increased amount of this phase forming. The DSC results are in reasonably good agreement with the Thermo-Calc predictions for all four alloys. However, no peaks corresponding to the formation of $Al_{13}Fe_4$ and Mg_2Si phases were observed in the DSC traces indicating the amount solidifying being marginal.

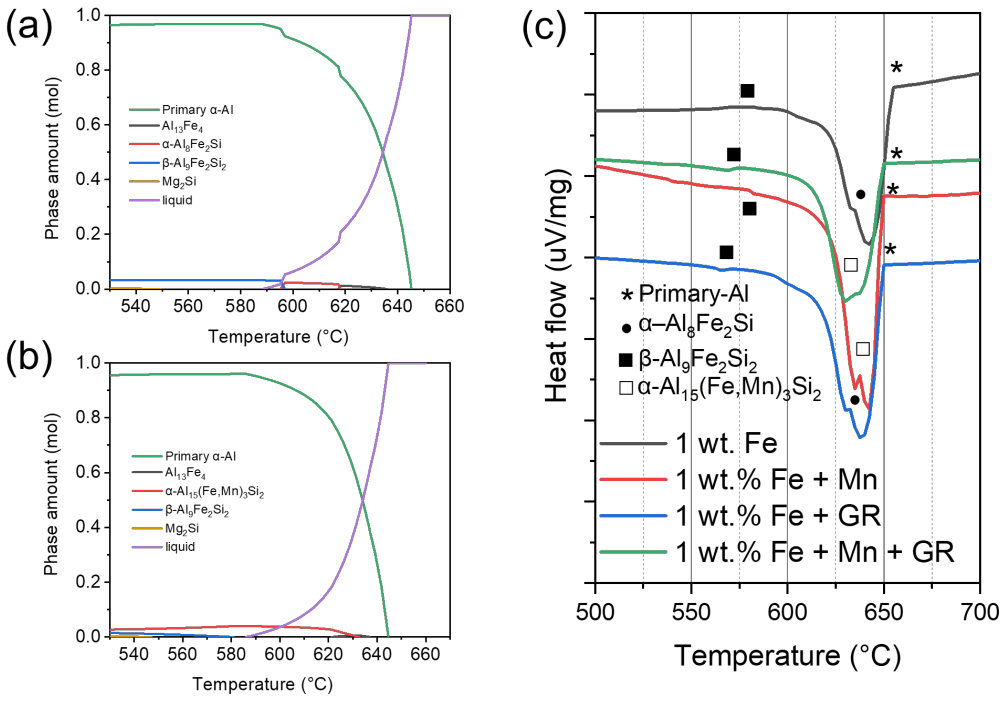

Fig. 8. Evolution of predicted phase fractions as a function of temperature, calculated through Thermo-Calc software, for (a) 1.0 wt.% Fe and (b) 1.0 wt.% Fe - 0.5 wt.% Mn alloy. DSC heat flow curves obtained during cooling are presented in (c) for 1.0 wt.% Fe containing alloys.

4. Discussion

In this study, the model 6082 wrought Al alloy with varying amounts of Fe, Mn and Al-5Ti-1B additions are solidified under different cooling rates to investigate the effect of alloying addition and cooling rate on the primary grain structure and Fe-IMC evolution. The experimental results suggest that solute influence grain size and the size, morphology, fraction and interconnectivity of IMCs. All of these features have important contribution to the overall microstructure, mechanical performance and downstream processability of alloys.

Fig. 3 clearly demonstrates that primary-Al grain size gradually decreases with Fe content and decreases further with Mn addition. The effect is prominent in the slow cooled region (steeper slope in Fig. 3b) but also noticeable under fast cooling. The largest reduction in grain size is observed under inoculation, especially under slow cooling rate where the grain size reduction after inoculation is substantial. The reduction in primary-Al grain size can be contributed by the effect of solute and the presence of potent nucleant or a combination of both. Solute effect on grain size reduction is traditionally explained through growth restriction theory [41-43]. The growth restriction factor (GRF) of a solute (Q) is expressed using phase diagram parameters as:

$$Q = mC_0(k-1) \quad (2)$$

where m is the gradient of the liquidus line, C_0 is the solute concentration in the bulk alloy and k is the partition coefficient. A high GRF leads to preferential segregation of solute at the solid-liquid interface leading to suppression in solid growth and refinement in grain size. The interdependence theory [44] suggested that the final grain size is inversely related to the GRF (Q) of the alloy, this is described by Equation (2):

$$d_{gs} = a + \frac{b}{Q} \quad (3)$$

where d_{gs} is the final grain size and a and b are parameters linked to the nucleation of grains , such as number of active nucleants and their potency. Accordingly, Fe segregation ahead of primary-Al solid/liquid interface leads to strong growth restriction and reduction in primary grain size as observed in Fig. 3. The effect is stronger during slow cooling due to the diffusion of Fe out of the solid into the liquid ahead while fast cooling may trap some Fe in the primary-Al. Further refinement in the primary-Al grain structure in the alloys containing Mn can be attributed to the additional growth restriction effect of Mn.

Cooling curves recorded during solidification of the alloys are presented in Fig. 9. There is a clear reduction in the maximum undercooling observed for Al solidification as a function of Fe (and Mn) content. In addition to this, inoculation leads to further (highest observed) reduction in the maximum undercooling as evidenced in Fig. 9. The initiation temperature for Al-nucleation can be determined from the deflection in the slope of the cooling curve that can be measured through the first derivative of temperature vs time in the cooling curves. As shown in Fig. 9b, nucleation is represented by peaks in the derivative of the cooling curve. The measured primary-Al nucleation temperatures for all seven alloys show a shift in the nucleation temperature from 641 °C to 649 °C due to the addition of solute elements or nucleating particles (TiB_2 inoculation). Solidification temperatures for various phases calculated using Thermo-Calc and identified from DSC scans are presented in Table 2 along with the nucleation temperatures measured from the cooling curves. While the highest rise in nucleation temperature is observed under Al-Ti-B inoculation as expected due to the presence of potent nucleating particles (TiB_2), there is a steady increase in the Al nucleation temperature with Fe content. This is contrary to the expected decrease in Al solidification temperature with Fe (due to the eutectic nature of Al-Fe system) as predicted by Thermo-Calc (Table 2). This suggests enhancement of heterogeneous nucleation of primary-Al with Fe addition but cannot be attributed to formation of any potent nucleating agent for Al. As solidification of primary-Al precedes Fe-IMC formation, there is no contribution to Al nucleation from such intermetallics. The nucleation enhancement with Fe addition is likely contributed by strong constitutional undercooling created ahead of the solid-liquid interface by the rejected Fe solute that allows fresh nucleation on indigenous nucleating particles. Mn appears to have limited influence on the Al nucleation temperature.

Formation of Fe-IMCs in Al-alloys containing Si, Mg, Mn is quite complex and varied. Many different Fe-containing intermetallic phases have been reported forming through various reaction during solidification, such as direct solidification, peritectic and eutectic reactions [8, 11, 23, 30, 45-48]. Si content and cooling rate largely affect the nature of intermetallic formed and their solidification morphologies [49-51]. In 6xxx series of dilute Al-Si-Mg alloys, the metastable hexagonal α–Al_8Fe_2Si and the monoclinic β-$Al_9Fe_2Si_2$ IMCs are stated to be the most common Fe-IMC formed through eutectic reactions late during solidification [33]. These IMCs are also predicted in the current alloys as shown in Fig. 8 from the Thermo-Calc simulations and verified through DSC (Fig. 8) and microstructural observations (Figs. 4, 5). For the alloys without Mn, α–Al_8Fe_2Si was not observed in the microstructure suggesting that

this phase dissolves during the eutectic solidification of β- IMCs as predicted by Thermo-Calc. Increase in Fe content increases the β-IMC fraction in the microstructure as expected but also leads to larger platelets as seen in Fig. 6. It has been suggested that nucleation of monoclinic β-$Al_9Fe_2Si_2$ is difficult, so increased Fe may have contributed to growth of nucleated IMCs rather than nucleation of more particles.

Addition of Mn has been stated to convert β-$Al_9Fe_2Si_2$ into α–$Al_{15}(Fe,Mn)_3Si_2$ IMCs [12-14]. A minimum Mn/Fe ratio of 0.5 is often suggested for complete conversion. For the 1Fe-0.5Mn alloys investigated in the present work some β-$Al_9Fe_2Si_2$ IMCs are present in the microstructure though α-$Al_{15}(Fe,Mn)_3Si_2$ constitute the major Fe-IMC. The formation of small amount of β-$Al_9Fe_2Si_2$ IMC is predicted by Thermo-Calc (Fig. 8b) and its nucleation can be observed in the DSC trace (Fig. 8c) and the derivative of the cooling curve (Fig. 9b). It has also been shown that the Mn/Fe ratio necessary for complete conversion of β- to α-IMC is heavily dependent on the cooling rate. Slow cooling has been suggested to favour β- IMC formation necessitating a higher Mn/Fe ratio (often ≥ 1) for complete suppression of β -IMC formation [51]. Our results from the slow cooled region of Mn containing alloy samples agree with this observation. While Mn addition is intended to promote less harmful α-$Al_{15}(Fe,Mn)_3Si_2$ over the detrimental β-$Al_9Fe_2Si_2$, Thermo-Calc prediction (Fig. 8b) suggests a solid-state reversion of β - to α -IMC following solidification in the Mn containing alloy. The final microstructure shows predominantly α–$Al_{15}(Fe,Mn)_3Si_2$ with minor β-IMC suggesting conversion of β - to α -IMC even if thermodynamically preferable, is negligible due to restricted diffusion during cooling. The β-IMC observed in the microstructure forms during the last stage of solidification rather than any solid-state transformation. It is noted, however, that although Mn addition minimises β-IMC, the overall fraction of IMCs in the microstructure increases as seen in Fig. 6c. This has also been reported in previous work that Mn increases the overall Fe-IMC content in the solidified Al-Si based alloys.

The effect of grain refinement on the evolution of Fe-IMCs is less investigated and understood. It has previously been reported in a model 6xxx alloy that the predominant intermetallic in the microstructure changed from cubic α-IMC to β-IMC following inoculation with Al-2Ti-1B and Al-5Ti-1B master alloys [33]. However, in the present work, addition of Al-5Ti-1B appears to reintroduce some α-$Al_{15}(Fe,Mn)_3Si_2$ in the β-$Al_9Fe_2Si_2$dominated microstructure in the 1%Fe alloy as evidenced in Figs. 4 and 5. For both 1Fe and 1Fe-0.5Mn alloys, inoculation also appears to refine the Fe-IMC particle sizes as shown in Figs. 6a and b. It has been suggested that unused TiB_2 particles from Al-Ti-B inoculation may cluster at primary-Al surface and

catalyse nucleation of α- and β–IMCs from the interdendritic liquid [33]. Nucleation temperatures measured from the cooling curves (Table 2) in the present wok indicate higher nucleation temperatures for the Fe-IMCs with the addition of grain refiner. This may suggest inoculant particles available in the interdendritic liquid assist heterogeneous nucleation of Fe-IMCs during the eutectic reactions agreeing with the previous report [33]. Although there are some discrepancies with the DSC results, cooling curve derived nucleation temperatures are more accurate representation of actual nucleation temperature. It is, however, not known if soluble Ti from the grain refiner changes the solidification temperature of IMCs. Nevertheless, the refinement of Fe-IMC particle size under inoculation is contributed by the refinement of primary-Al grain structure rather than any enhancement in the nucleation of the IMCs catalysed by inoculation.

The deep-etched microstructures micrograph indicated that majority of the Fe-IMC particles are located on primary-Al grain boundary. Accordingly, primary-Al grain structure plays an imperative role on the development of Fe-IMCs later during their solidification through eutectic reaction. Fig. 10 schematically illustrates the evolution of Fe-IMCs in the eutectic liquid pockets between primary-Al grains. Both α-$Al_{15}(Fe,Mn)_3Si_2$ and β-$Al_9Fe_2Si_2$, solidify in the large and scattered interdendritic liquid pockets in the base alloy ingots leading to growth of long plates (β) or dendritic (α) morphologies (Fig. 10a). Following inoculation, the development of fine equiaxed primary-Al grain structure leads to well distributed but smaller intergranular liquid pockets. Consequently, the Fe-IMCs nucleated in these intergranular liquid pockets have limited growth space leading to finer particle size in the inoculated alloys as shown schematically in Fig. 10b. Any contribution to nucleation of the Fe-IMCs from the TiB_2 particles available in the intergranular liquid, as suggested from the cooling curve analysis, can further aid the refinement of such particles. Inoculation is, thereby, beneficial not only in refining the primary Al-grain structure but also potentially limiting the size of harmful Fe-IMCs and also converting some into less detrimental form. This could be particularly beneficial in Alloys with high Fe impurity content where detrimental plate-type β-$Al_9Fe_2Si_2$ IMCs are prevalent.

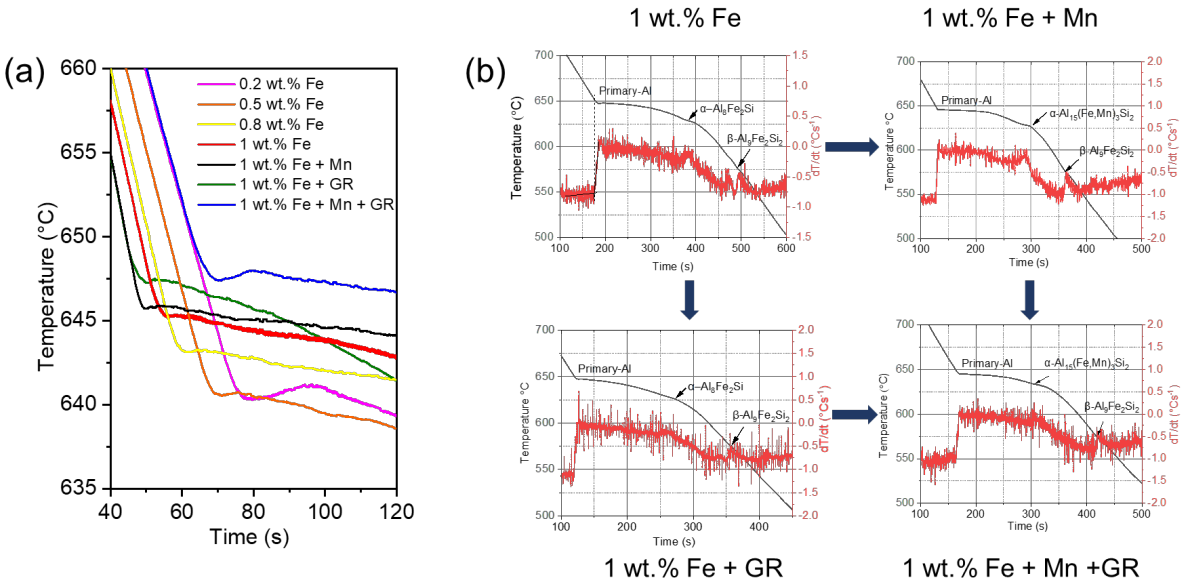

Fig. 9. Cooling curves measured during solidification showing (a) primary-Al nucleation for all seven alloys and (b) the time derivative of cooling curves showing the primary-Al and intermetallic nucleation in 1.0 wt. %Fe alloys with Mn, grain refiner (GR), and Mn and GR addition.

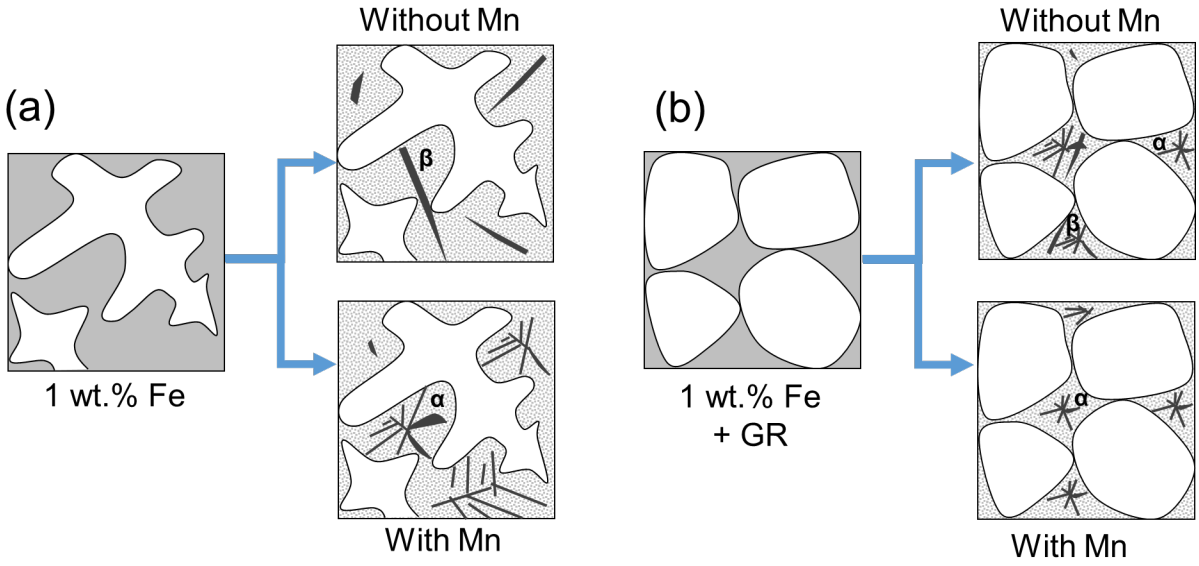

Fig. 10. Schematic illustration of the microstructure evolution for (a) non inoculated and (b) inoculated 1.0 wt. % Fe alloy with and without Mn addition.

Table 2. Phase transformation and nucleation temperature for major phases from Thermo-Calc calculation, DSC and Cooling curve measurements.

Alloy designation	Phase transformation/ nucleation temperature (°C)											
	Primary-Al			α-Al_8Fe_2Si			α-$Al_{15}(Fe,Mn)_3Si_2$			β-$Al_9Fe_2Si_2$		
	Property	DSC	Cooling Curve	Property	DSC	Cooling Curve	Property	DSC	Cooling Curve	Property	DSC	Cooling Curve
0.2Fe	643	640	641	617	628	620	-	-	-	583	581	578
0.5Fe	646	653	641	617	628	621	-	-	-	584	580	578
0.8Fe	645	653	645	618	630	621	-	-	-	588	581	579
1Fe	645	653	645	618	634	626	-	-	-	596	583	580
1Fe - Mn	644	650	647	-	-	-	633	635	628	582	585	584
1Fe + GR	647	650	648	628	635	630	-	-	-	597	573	585
1Fe - Mn + GR	647	650	649	-	-	-	632	628	633	582	575	578

5. Conclusions

Microstructure evolution in a model 6082 alloy with varying Fe level from 0.2 to 1.0 wt.% is investigated under slow and fast cooling in a wedge-shaped mould and evaluated using Thermo-Calc, DSC and cooling curve analysis, and microstructure characterisation. The effect of 0.5 wt.% Mn addition and inoculation using Al-5Ti-1B grain refiner is also investigated. The following conclusions can be drawn from the experimental results:

(1) Increase in solute content in the form of Fe and Mn refined the dendritic grain structure formed in the base alloy from the growth restriction effect of solute. Increased Fe content also resulted in a reduction in the nucleation undercooling for primary-Al suggesting constitutional undercooling driven enhancement to heterogeneous nucleation.

(2) Finest and equiaxed grain structure is observed in the inoculated alloys, especially under slow cooling, due to potent nucleants leading to the lowest observed nucleation undercooling for primary-Al. Addition of Mn had minimal effect on the grain refining efficiency of inoculant.

(3) β–$Al_9Fe_2Si_2$ intermetallic is prevalent in the final microstructure of Fe containing alloys with the particle size and area fraction increasing steadily with Fe content. Thermo-Calc predicts solidification of metastable α–Al_8Fe_2Si earlier and its dissolution concurrent with β–formation, both intermetallics solidifying through eutectic reaction. DSC and cooling curve analysis show solidification peaks for both intermetallics.

(4) 0.5 wt.% Mn addition leads to α-$Al_{15}(Fe,Mn)_3Si_2$ being the major intermetallic phase solidifying in the 1.0 wt.% Fe containing alloy though some β–$Al_9Fe_2Si_2$ remained, especially under slow cooling and predicted by Thermo-Calc simulation. Mn addition leads to an overall increase in Fe-intermetallic fraction in the microstructure.

(5) Al-5Ti-1B inoculation retains some α–Al_8Fe_2Si in the microstructure of 1.0 wt.%Fe alloy without Mn addition. The intermetallic particle size reduced upon inoculation in alloys with or without Mn addition contributed by the reduction in the intergranular liquid pocket size and enhancement of intermetallic nucleation as evidenced from cooling curve analysis.

Declaration of competing interest

The authors declare that they have no known competing financial interests or personal relationships that could have appeared to influence the work reported in this paper.

CRediT authorship contribution statement

M. H. Khan: Writing - original draft, Conceptualization, Methodology, Validation, Investigation. **A. Das**: Formal analysis, Supervision, Writing – review & editing. **Z. Li**: Supervision, Writing – review & editing. **H. R. Kotadia**: Conceptualization, Methodology, Formal analysis, Supervision, Writing – review & editing.

Acknowledgment

This research was funded by the Industrial Cooperative Awards in Science & Technology (CASE) (voucher no. 17000037). In addition to that, the characterisation facility is supported from the Higher Education Funding Council for England (HEFCE) fund and the WMG Centre High Value Manufacturing Catapult is gratefully acknowledged.

References

[1] I. Polmear, Light Alloys: From Traditional Alloys to Nanocrystals, 4th Edition, Butterworth-Heinemann (2005).
[2] W.S. Miller, L. Zhuang, J. Bottema, A.J. Wittebrood, P. De Smet, A. Haszler, A. Vieregge, Recent development in aluminium alloys for the automotive industry, Materials Science and Engineering: A 280(1) (2000) 37-49.
[3] G. Gaustad, E. Olivetti, R. Kirchain, Improving aluminum recycling: A survey of sorting and impurity removal technologies, Resources, Conservation and Recycling 58 (2012) 79-87.
[4] A.K. Das, Designing aluminium alloys for a recycling friendly world, Materials Science Forum 519-521 (2006) 1239-1244.
[5] P.A. Enkvist, P. Klevnas, The Circular Economy—A Powerful Force for Climate Mitigation, Material Economics Sverige (2018).
[6] D. Raabe, C.C. Tasan, E.A. Olivetti, Strategies for improving the sustainability of structural metals, Nature 575(7781) (2019) 64-74.
[7] J. Davis, ASM Specialty Handbook: Aluminum and Aluminum Alloys, ASM International (1993).
[8] N.A. Belov, A.A. Aksenov, D.G. Eskin, Iron in Aluminium Alloys : Impurity and Alloying Element, CRC Press, Taylor & Francis Ltd (2002).
[9] H.W.L. Phillips, Annotated Equilibrium Diagrams of Some Aluminium Alloy Systems, The Institute of Metals, London (1959).
[10] J.Z. Yi, Y.X. Gao, P.D. Lee, T.C. Lindley, Effect of Fe-content on fatigue crack initiation and propagation in a cast aluminum–silicon alloy (A356–T6), Materials Science and Engineering: A 386(1) (2004) 396-407.
[11] J. Wang, P.D. Lee, R.W. Hamilton, M. Li, J. Allison, The kinetics of Fe-rich intermetallic formation in aluminium alloys: In situ observation, Scripta Materialia 60(7) (2009) 516-519.
[12] S. Murali, K.S. Raman, K.S.S. Murthy, Effect of trace additions (beryllium, chromium, manganese and cobalt) on the mechanical properties and fracture toughness of iron-containing Al-7Si-0.3Mg alloy, Ljevarstvo 37 (1995) 3-14.
[13] M.H. Mulazimoglu, A. Zaluska, J.E. Gruzleski, F. Paray, Electron microscope study of Al-Fe-Si intermetallics in 6201 aluminum alloy, Metallurgical and Materials Transactions A 27(4) (1996) 929-936.

[14] S.G. Shabestari, The effect of iron and manganese on the formation of intermetallic compounds in aluminum–silicon alloys, Materials Science and Engineering: A 383(2) (2004) 289-298.
[15] A. Das, H.R. Kotadia, Effect of high-intensity ultrasonic irradiation on the modification of solidification microstructure in a Si-rich hypoeutectic Al–Si alloy, Materials Chemistry and Physics 125(3) (2011) 853-859.
[16] H.R. Kotadia, M. Qian, A. Das, Microstructural modification of recycled aluminium alloys by high-intensity ultrasonication: Observations from custom Al–2Si–2Mg–1.2Fe–(0.5,1.0)Mn alloys, Journal of Alloys and Compounds 823 (2020) 153833.
[17] C. Lin, S.-s. Wu, G. Zhong, L. Wan, P. An, Effect of ultrasonic vibration on Fe-containing intermetallic compounds of hypereutectic Al–Si alloys with high Fe content, Transactions of Nonferrous Metals Society of China 23(5) (2013) 1245-1252.
[18] H.R. Kotadia, N. Hari Babu, H. Zhang, S. Arumuganathar, Z. Fan, Solidification Behavior of Intensively Sheared Hypoeutectic Al-Si Alloy Liquid, Metallurgical and Materials Transactions A 42(4) (2011) 1117-1126.
[19] H.R. Kotadia, J.B. Patel, H.T. Li, F. Gao, Z. Fan, Microstructure Evolution in Melt Conditioned Direct Chill (MC-DC) Casting of Fe-Rich Al-Alloy, Advanced Materials Research 1019 (2014) 90-95.
[20] H.R. Kotadia, N. Hari Babu, H. Zhang, Z. Fan, Microstructural refinement of Al–10.2%Si alloy by intensive shearing, Materials Letters 64(6) (2010) 671-673.
[21] S. Nafisi, D. Emadi, M.T. Shehata, R. Ghomashchi, Effects of electromagnetic stirring and superheat on the microstructural characteristics of Al–Si–Fe alloy, Materials Science and Engineering: A 432(1) (2006) 71-83.
[22] Y. Osawa, S. Takamori, T. Kimura, K. Minagawa, H. Kakisawa, Morphology of Intermetallic Compounds in Al-Si-Fe Alloy and Its Control by Ultrasonic Vibration, MATERIALS TRANSACTIONS 48(9) (2007) 2467-2475.
[23] A.N. Lakshmanan, S.G. Shabestari, J.E. Gruzleski, Microstructure control of iron intermetallics in Al-Si casting alloys, Z. Metallkd. 86(7) (1995) 457-67.
[24] A.M. Samuel, A. Pennors, C. Villeneuve, F.H. Samuel, H.W. Doty, S. Valtierra, Effect of cooling rate and Sr-modification on porosity and Fe-intermetallics formation in Al-6.5% Si-3.5% Cu-Fe alloys, International Journal of Cast Metals Research 13(4) (2000) 231-253.
[25] L.A. Narayanan, F.H. Samuel, J.E. Gruzleski, Dissolution of iron intermetallics in Al-Si Alloys through nonequilibrium heat treatment, Metallurgical and Materials Transactions A 26(8) (1995) 2161-2174.
[26] C.M. Allen, K.A.Q. O'Reilly, B. Cantor, P.V. Evans, Intermetallic phase selection in 1XXX Al alloys, Progress in Materials Science 43(2) (1998) 89-170.
[27] M. Mahta, M. Emamy, A. Daman, A. Keyvani, J. Campbell, Precipitation of Fe rich intermetallics in Cr- and Co-modified A413 alloy, International Journal of Cast Metals Research 18(2) (2005) 73-79.
[28] T. Gao, K. Hu, L. Wang, B. Zhang, X. Liu, Morphological evolution and strengthening behavior of α-Al(Fe,Mn)Si in Al–6Si–2Fe–xMn alloys, Results in Physics 7 (2017) 1051-1054.
[29] P. Ashtari, H. Tezuka, T. Sato, Influence of Sr and Mn additions on intermetallic compound morphologies in Al-Si-Cu-Fe cast alloys, Materials Transactions 44(12) (2003) 2611-2616.
[30] W. Khalifa, F.H. Samuel, GM-NSERC-UQAC, J.E. Gruzleski, H.W. Doty, S. Valtierra, Nucleation of Fe-intermetallic phases in the Al-Si-Fe alloys, Metallurgical and Materials Transactions A 36(4) (2005) 1017-1032.
[31] X. Cao, J. Campbell, The nucleation of Fe-Rich phases on oxide films in Al-11.5Si-0.4Mg cast alloys, Metallurgical and Materials Transactions A 34(7) (2003) 1409-1420.

[32] Y.H. Cho, H.-C. Lee, K.H. Oh, A.K. Dahle, Effect of Strontium and Phosphorus on Eutectic Al-Si Nucleation and Formation of β-Al5FeSi in Hypoeutectic Al-Si Foundry Alloys, Metallurgical and Materials Transactions A 39(10) (2008) 2435-2448.
[33] A. Lui, P.S. Grant, I.C. Stone, K.A.Q. O'Reilly, The Role of Grain Refiner in the Nucleation of AlFeSi Intermetallic Phases During Solidification of a 6xxx Aluminum Alloy, Metallurgical and Materials Transactions A 50(11) (2019) 5242-5252.
[34] E. Taghaddos, M.M. Hejazi, R. Taghiabadi, S.G. Shabestari, Effect of iron-intermetallics on the fluidity of 413 aluminum alloy, Journal of Alloys and Compounds 468(1) (2009) 539-545.
[35] P.A. Karnezis, G. Durrant, B. Cantor, Characterization of Reinforcement Distribution in Cast Al-Alloy/SiCp Composites, Materials Characterization 40(2) (1998) 97-109.
[36] R.N. Corby, P.J. Black, The structure of α-(AlFeSi) by anomalous-dispersion methods, Acta Crystallographica Section B 33(11) (1977) 3468-3475.
[37] M. Cooper, The crystal structure of the ternary alloy [alpha](AlFeSi), Acta Crystallographica 23(6) (1967) 1106-1107.
[38] G. Phragmen, On the Phases Occurring in Alloys of Aluminum with Copper, Magnesium, Manganese, Iron and Silicon, J. Inst. Metals (London) 77 (1950) 489–552.
[39] L.F. Mondolfo Aluminum Alloys: Structure and Properties, Butterworths (1976).
[40] C. Rømming, V. Hansen, J. Gjønnes, Crystal structure of β-Al4.5FeSi, Acta Crystallographica Section B 50(3) (1994) 307-312.
[41] J.A. Spittle, Grain refinement in shape casting of aluminium alloys, International Journal of Cast Metals Research 19(4) (2006) 210-222.
[42] M. Easton, D. StJohn, Grain refinement of aluminum alloys: Part I. the nucleant and solute paradigms—a review of the literature, Metallurgical and Materials Transactions A 30(6) (1999) 1613-1623.
[43] Y.C. Lee, A.K. Dahle, D.H. StJohn, The role of solute in grain refinement of magnesium, Metallurgical and Materials Transactions A 31(11) (2000) 2895-2906.
[44] D.H. StJohn, M. Qian, M.A. Easton, P. Cao, The Interdependence Theory: The relationship between grain formation and nucleant selection, Acta Materialia 59(12) (2011) 4907-4921.
[45] S.J. Maggs, PhD Thesis: Intermetallic Phase Selection in Dilute AI-Fe-Si alloys, The University of Leeds, School of Materials (1996).
[46] S. Kumar, P.S. Grant, K.A.Q. O'Reilly, Evolution of Fe Bearing Intermetallics During DC Casting and Homogenization of an Al-Mg-Si Al Alloy, Metallurgical and Materials Transactions A 47(6) (2016) 3000-3014.
[47] Z. Que, Y. Wang, Z. Fan, Formation of the Fe-Containing Intermetallic Compounds during Solidification of Al-5Mg-2Si-0.7Mn-1.1Fe Alloy, Metallurgical and Materials Transactions A 49(6) (2018) 2173-2181.
[48] J.A. Taylor, Iron-Containing Intermetallic Phases in Al-Si Based Casting Alloys, Procedia Materials Science 1 (2012) 19-33.
[49] Z. Zhang, H. Tezuka, E. Kobayashi, T. Sato, Effects of the Mn/Fe Ratio and Cooling Rate on the Modification of Fe Intermetallic Compounds in Cast A356 Based Alloy with Different Fe Contents, MATERIALS TRANSACTIONS 54(8) (2013) 1484-1490.
[50] Y. Zhang, Y. Liu, Y. Han, C. Wei, Z. Gao, The role of cooling rate in the microstructure of Al–Fe–Si alloy with high Fe and Si contents, Journal of Alloys and Compounds 473(1) (2009) 442-445.
[51] E. Cinkilic, C.D. Ridgeway, X. Yan, A.A. Luo, A Formation Map of Iron-Containing Intermetallic Phases in Recycled Cast Aluminum Alloys, Metallurgical and Materials Transactions A 50(12) (2019) 5945-5956.